11-2020

Simulations and Experiments Reveal Effect of Nanopores on Helium Diffusion in Quartz

Rustin Domingos

Marissa M. Tremblay

David L. Shuster

Burkhard Militzer

Simulations and experiments reveal effect of nanopores on helium diffusion in quartz

Rustin Domingos[1,*], Marissa M. Tremblay[2], David L. Shuster[1,3], and Burkhard Militzer[1,4]

[1]Department of Earth and Planetary Science, University of California, Berkeley, Berkeley, CA 94720, USA
[2]Department of Earth, Atmospheric, and Planetary Sciences, Purdue University, West Lafayette, IN 47907, USA
[3]Berkeley Geochronology Center, Berkeley, CA 94709, USA
[4]Department of Astronomy, University of California, Berkeley, Berkeley, CA 94720, USA
*corresponding author: rustindomingos@gmail.com

ABSTRACT
The diffusion properties of noble gases in minerals are widely utilized to reconstruct the thermal histories of rocks. Here, we combine density functional theory (DFT) calculations with laboratory experiments to investigate controls on helium diffusion in quartz. DFT calculations for perfect α-quartz predict substantially lower activation energies and frequency factors for helium diffusion than observed in laboratory experiments, especially in the [001] direction. These results imply that no helium could be retained in quartz at Earth surface temperatures, which conflicts with observations of partial cosmogenic ^{3}He retention over geologic timescales. Here, we implement a model of helium diffusion in α-quartz modulated by nanopore defects that disrupt energetically-favorable diffusion pathways. In this model, we find that laboratory-determined diffusivities can be most closely reproduced when a helium atom encounters ~70 nanopore sites per million interstitial sites. The results of our model indicate that diffusion of helium in natural quartz, like other noble gases in other minerals, can be significantly modulated by extended defects.

KEYWORDS
helium; quartz; diffusion; density functional theory; nanopores

INTRODUCTION
Isotopic systems that record information about the thermal evolution of materials, known as thermochronometers, are used extensively to understand processes occurring on Earth and other planetary bodies.[1] Many thermochronometers utilize the production and thermally-activated diffusion of radiogenic ^{4}He in minerals. Recently, the diffusive loss of cosmogenic ^{3}He in quartz has been developed as an Earth surface thermochronometer, with potential applicability in reconstructing past climate conditions.[2]

Quantitative applications of helium-based thermochronometers require knowledge of the kinetics of helium diffusion in a particular mineral. Diffusion parameters defining an Arrhenius-type relationship are most often quantified empirically by laboratory experiments, either by performing incremental helium degassing (e.g., Shuster and Farley[3]; Figure 1) or helium diffusion/implantation measurements at grain surfaces (e.g., Cherniak et al.[4]). Sometimes, noble gas diffusion behavior observed in experiments can be readily linked to imperfections in the crystal structure. For example, experiments on the minerals apatite and zircon empirically

demonstrate that radiation damage decreases helium diffusivity below a threshold damage density.[5–9] Radiation damage density can either be measured directly via Raman spectroscopy, in the case of zircon, or estimated from measured concentrations of the damage-inducing elements U and Th and thermal history modeling. Extended defects are also present in minerals, but it is more challenging to investigate their effects on helium diffusion kinetics experimentally because we lack a readily quantifiable proxy for defect density. In contrast, the effects of defects on diffusion kinetics can be predicted using density functional theory (DFT) to reveal information about diffusion mechanisms and sources of kinetics variability that cannot be inferred from laboratory experiments alone. For example, DFT calculations have been used to demonstrate that vacancy-type defects can slow helium diffusivities in apatite and zircon.[10–12]

We undertook DFT calculations and experiments to investigate helium diffusion kinetics in quartz. Previous experimental studies find activation energies for helium diffusion ranging between ~70 and 100 kJ/mol.[3,13] For example, Figure 1 shows helium diffusivities calculated from experiments on a gem-quality quartz specimen, for which we find an activation energy of 84.5 kJ/mol. This is substantially higher than activation energies predicted from previous DFT calculations for helium diffusion in perfect quartz crystals, which range from ~20 to 51 kJ/mol.[14] Our DFT calculations confirm these low activation energies. We also calculate frequency factors for helium diffusion in perfect quartz that are substantially lower than those determined experimentally. We use the nanopore in our simulations as a proxy for extended defects in quartz more generally that, like a nanopore, may act as local energy traps for helium atoms.

METHODS
DFT Calculations
Defect-free α-Quartz Activation Energy
To calculate activation energies for ^{3}He diffusion in defect-free α-quartz, we generated a 2 x 2 x 2 α-quartz supercell with 72 atoms (Figure 2) and carried out ionic relaxation in the density functional theory framework as implemented in the Vienna *ab initio* simulation package.[15] After initial relaxation, we placed a ^{3}He atom at different interstitial sites and found that they relaxed into interstitial sites that lie in channels that run parallel to the c-axis of the unit cell.

We calculated the activation energy as the energy barrier the helium atom must overcome to migrate from one interstitial site to an identical site nearby in the crystal. To calculate this barrier, we use the climbing image nudged elastic band method (ci-NEB).[16–18] The NEB method uses a chain of states that are connected by spring forces and tied to two fixed end points. Endpoints of the NEB are the translationally symmetric images of the relaxed interstitial sites. Intermediate images are generated by linearly interpolating between the two endpoints. All atomic positions of all states are relaxed until the minimum energy path (MEP) is found. The climbing image modification of NEB removes the spring forces of the highest energy image, inverts the true forces on the image, and allows the image to climb higher in energy along the MEP to the saddle point, which allows us to determine the saddle point with fewer images than would be needed in the original NEB implementation. We calculated MEPs using the ci-NEB method with a spring constant of -5eV/Å between neighboring images (Figure 3).

Nanopore Activation Energy

To calculate activation energies for ^{3}He to leave a nanopore in a α-quartz crystal, we created a nanopore in a 135 atom α-quartz supercell by removing 4 silicon and 10 oxygen atoms inside a sphere of radius 3.275Å (Figure 2). The number of atoms removed was sufficiently small to maintain the integrity of the remaining structure when the nanopore is created. The structure was subsequently relaxed to ensure the persistence of the nanopore, as well as the structural integrity of the quartz crystal including its c-axis channels. Interstitial ^{3}He endpoint images were placed in all intact c-axis interstitial sites and relaxed. Intermediate images were generated between the initial state of the helium atom relaxed in the nanopore and the endpoint images.

For the nanopore scenario, we calculated the activation energy as the barrier the helium atom must overcome to migrate from inside the nanopore to an interstitial c-axis site that remained intact in the crystal. This barrier was calculated using the ci-NEB method, as was done in the perfect crystal (Figure 3).

Diffusion Coefficients

With knowledge of the initial minimum state and transition state at the saddle point, we calculate the frequency factor D_0 through analysis of the harmonic frequencies of the normal modes of the initial state and transition state[19] as:

$$D_0 = \frac{\nu_1 \nu_2 \nu_3}{\nu_1^* \nu_2^*} a^2 \qquad \text{(Eq. 1)}$$

where ν_i^* are the real eigen-frequencies at the saddle point, ν_i are the real eigen-frequencies at the initial state and a is the hopping distance between sites.

Insertion Energy

The insertion energy E_{ins}, is computed as the difference between the energy of the structure with interstitial ^{3}He and the sum of the energies of perfect quartz and an isolated ^{3}He atom ($E_{ins} = E_{He+quartz} - (E_{quartz} + E_{He})$). Calculation of this value gives us the maximal trapping energy in the limit of very large nanopores.

Diffusion experiment

We conducted a stepwise diffusion experiment on sample GRR-1668, a gem quality, optically clear, single prismatic quartz crystal from Conselheiro Mata, Minas Gerais, Brazil. The diffusion kinetics of ^{3}He, ^{4}He, and ^{21}Ne in GRR-1668 were previously measured and reported by Shuster and Farley[3], who observed simple, linear Arrhenius behavior for all three isotopes (Fig. 1). We irradiated additional material from GRR-1668 with protons at the Francis H. Burr Proton Therapy Center at the Massachusetts General Hospital in June 2017. Tremblay et al.[13] provide a detailed description of the proton irradiation setup. This irradiation used 228 MeV protons and had a total fluence of 9.99 × 10^{15} protons/cm^2. Following irradiation, we selected a single irradiated fragment of GRR-1668 for our experiment. This fragment was devoid of any cracks or inclusions, as determined from inspection under a stereomicroscope, and had a spherical equivalent radius of 260 μm.

The step-degassing experiment followed the methods described in Tremblay et al.[13] and are briefly summarized here. We placed the selected grain in a PtIr alloy packet in direct contact with a 0.13 mm diameter, bare-wire K-type thermocouple. We mounted the packet–thermocouple assembly inside an ultra-high vacuum microfurnace, such that the packet was suspended from the K-type thermocouple. We used a 70W diode laser in feedback control with the thermocouple to heat the packet to a setpoint temperature; we achieved the setpoint within 30 seconds of starting a heating step and maintained the temperature to within 2 ℃ of the setpoint for the remainder of the heating step. The gas extracted from a heating step was purified and analyzed on an MAP-215-50 sector field mass spectrometer at the Berkeley Geochronology Center; Tremblay et al.[13] describe the gas purification and analytical procedures in detail.

Heating steps continued until numerous successive steps had He signals below what we were able to detect, which we determined by measuring room-temperature procedural blanks in between heating steps. We also measured aliquots of a manometrically-calibrated, ^{3}He-spiked He standard in between heating steps to determine He sensitivities during the experiment. Amounts of ^{3}He reported in Table 1 include propagated uncertainties from the blank corrections and sensitivity regression. We use these calculated ^{3}He amounts and the heating step durations to calculate diffusivities using the discretized equations in Fechtig and Kalbitzer[20] for a spherical diffusion geometry (Table 1).

RESULTS AND DISCUSSION
Diffusion experiment
The ^{3}He diffusion experiment we report here on gem-quality quartz sample GRR-1668 is characterized by simple, linear Arrhenius behavior and agrees well with the original ^{3}He diffusion experiment on this quartz reported by Shuster and Farley[3] (Figure 1). Combined, the two diffusion experiments yield an activation energy of 84.5 ± 0.6 kJ/mol and a pre-exponential factor of (1.5 ± 0.3) × 10^{-2} m^2s^{-1}. These kinetics parameters are within the range of those observed for different non-gem quality quartz samples previously studied.[13]

Comparison with DFT calculations
The insertion energy was determined to be 0.526eV, in agreement with previously DFT calculations with range 0.52-0.53eV[14]. This maximum trapping energy is 0.275eV larger than the nanopore used in our model. Calculated activation energies and frequency factors for ^{3}He diffusion in defect-free α-quartz simulations are shown in Table 2 for each crystallographic direction. We find the lowest activation energy of 21.8 kJ/mol in the [001] direction, suggesting that helium diffusion is strongly anisotropic and dominated by diffusion along the c-axis channels in the defect-free crystal structure. These calculated activation energies are consistent with previous DFT calculations[14] and are significantly lower than any activation energies observed in laboratory diffusion experiments (Figure 1). These DFT results indicate helium diffusivities at Earth surface temperatures are many orders of magnitude higher than expected from both laboratory experiments and geologic observations.

Table 2 also reports the lowest activation energy and frequency factor for ^{3}He diffusion out of the nanopore into a c-axis interstitial site. We find that the activation energy in this scenario is 82.9 kJ/mol, when considering our maximum trapping energy we calculate the maximum

activation in the limit of large nanopores to be 110 kJ/mol. This is comparable to activation energies observed in laboratory helium diffusion experiments reported here (Figure 1) and elsewhere[13]. However, the frequency factor is ~5 orders of magnitude lower than those typically observed in laboratory experiments.

The diffusion kinetics predicted by DFT calculations for ^{3}He in perfect quartz suggest much higher diffusivities at Earth surface temperatures (< 55 ºC) than determined by laboratory experiments (e.g., Figure 1), particularly along channels in the [001] direction for which no ^{3}He retention is predicted over any timescale. The diffusion kinetic parameters predicted for perfect quartz are inconsistent with observations demonstrating partial retention of cosmogenic ^{3}He in quartz in cold environments during the Quaternary period.[2,21] Taking our DFT results as accurate, this implies that natural quartz samples like those studied in laboratory experiments contain extended defects that deviate from the idealized quartz structure used in our DFT calculations, which play a fundamental role in modulating helium diffusion.

Our DFT simulation of helium diffusion in the presence of a nanopore supports this assertion; the activation energy that we calculate for a ^{3}He atom to migrate from the nanopore to an interstitial c-axis channel site is significantly higher than those calculated for defect-free quartz and is similar to activation energies we observe in incremental degassing experiments.[13] The bulk diffusivity in quartz containing nanopores at a particular temperature can be calculated as follows:

$$\frac{1}{D_{bulk}} = \frac{f_{nanopore}}{D_{nanopore}} + \frac{f_{[001]}}{D_{[001]}} \qquad \text{(Eq. 2)}$$

Where f is the fraction of diffusion steps out of either a nanopore or interstitial c-axis channel site ($f_{nanopore} + f_{[001]} = 1$), with $f_{nanopore}$ being the fraction of interstitial sites that are replaced by a nanopore site. Derivations of Eq. 2 have been detailed in Supplementary Information as well as independently by Gerin et al.[11] Here we consider just one size of nanopore as a proxy for a distribution of nanopore sizes with varying activations that contribute to an effective diffusion rate we see in experiment. In principle other diffusion directions, nanopore sizes, and types of defects could be considered, which would require additional terms in Eq. 2. Figure 4 compares the experimentally-observed diffusivities in quartz GRR-1668 with DFT-simulated diffusivities calculated according to Eq. 2 for different fractions of diffusion steps out of nanopores and in the [001] direction. We find that the following values of $f_{nanopore}$ minimize the reduced χ^2 deviation with the observed diffusivities in the laboratory experiments on gem-quality quartz sample GRR-1668: $(7.2 \pm 0.5) \times 10^{-5}$ for a spherical diffusion geometry (Figure 5), and $(9.9 \pm 1.3) \times 10^{-6}$ for an infinite sheet diffusion geometry (Table 3). Including diffusion in the [100] and [010] directions yields indistinguishable values of $f_{nanopore}$ (Table 3). Importantly, the laboratory observations cannot be explained by combinations of the [001], [100], and [010] directions in perfect quartz. A defect that disrupts diffusion along the c-axis channel, like the trapping phenomena simulated by nanopores, is required.

Watson and Cherniak[22] proposed that nanopores at crystal surfaces could cause anomalously high apparent Ar solubilities they sometimes observed in diffusive-uptake experiments on quartz.

They used a Fickian diffusion model with a sink term to further suggest that isolated nanopores impede argon diffusion in quartz but do not affect the overall diffusion length scale. These proposed effects of nanopores are broadly consistent with our laboratory experiments, which indicate that the diffusion length scale is defined by the physical grain size (Figure 1), and with our DFT simulations, which demonstrate nanopores impede helium diffusion in quartz (Figure 1, Table 2). We note, however, that the effect of nanopores on Ar diffusivities modeled by Watson and Cherniak[21] is small relative to the effect on He diffusivities modeled here, which may be related to the much larger size of Ar atoms. Moreover, the nanopores observed and modeled by Watson and Cherniak[22] were at least 30 times larger than the nanopores simulated here. In the limit of large nanopores we expect the trapping energy to approach the insertion energy.

CONCLUSIONS

Our DFT simulation was carried out for one type of nanopore geometry and size. The activation energies and frequency factors associated with migration from different types and sizes of extended defects, however, will likely vary. Considering that the types, sizes, and abundances of defects differ among natural quartz samples, this expected variability in diffusion parameters associated with different defects may explain why we observe a range of helium diffusion kinetic parameters in laboratory experiments on quartz, and perhaps even why we sometimes observe multiple diffusion domain-like behavior.[13]

This work supports growing evidence from intercomparisons of simulations and experiments that defects (e.g., Kovalenko et al.[23]) and other imperfections in the crystal structure (e.g., radiation damage[6]) play a fundamental role in modulating helium diffusion in a range of minerals. Like quartz, DFT simulations predict activation energies of helium diffusion in the [001] direction of defect-free apatite and zircon that are substantially lower than those observed experimentally.[24,25] Introducing defects into the apatite and zircon structure, as we have done here for quartz, increases the activation energy of helium diffusion to within the range observed experimentally.[10–12] The effects of defects on helium diffusion may explain why we observe dispersion in apatite and zircon (U-Th)/He datasets that cannot be explained by radiation damage effects alone.[10,26,27] For quartz and perhaps other minerals, this result supports the approach of measuring sample-specific helium diffusion kinetics via laboratory experiments advocated for by Tremblay et al.[13], as we expect diffusion kinetics to vary as a function of the type and density of defects present.

FIGURES AND TABLES
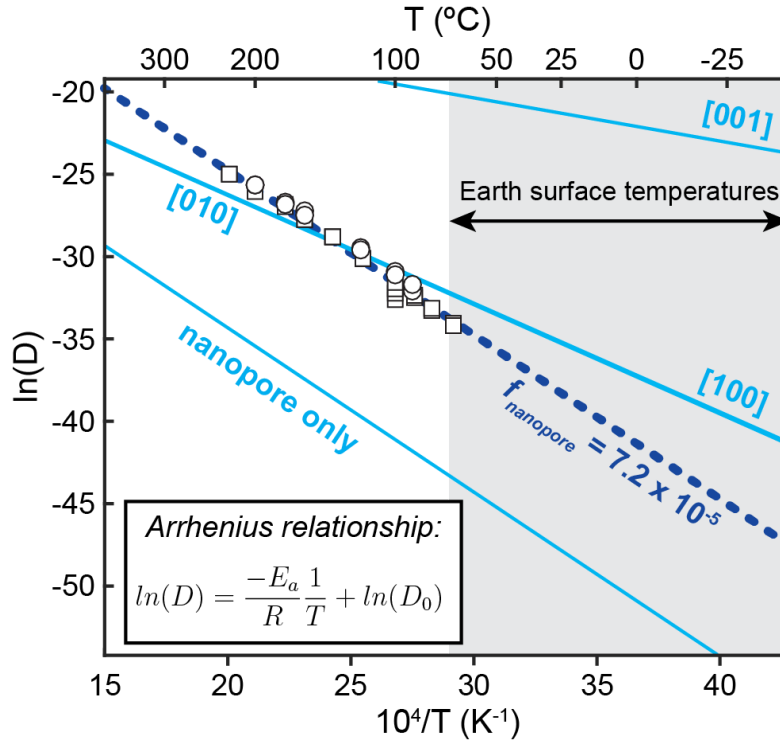
Figure 1: Arrhenius plot comparing helium diffusion kinetics in quartz predicted by DFT calculations (lines) and measured via laboratory experiments for a gem-quality quartz specimen (symbols). The activation energy E_a and frequency factor D_0, which control the dependence of diffusivity D on temperature T, define the slope and intercept, respectively, in this plotting space. R = gas constant. D values are normalized to m^2s^{-1}. Solid light blue = DFT calculations for particular crystallographic directions and the nanopore individually. Dashed dark blue = helium diffusivity in quartz in the presence of nanopores, where the fraction of diffusion steps out of nanopores ($f_{nanopore}$) minimizes the misfit with the experimental data. Squares = Shuster and Farley[3]; circles = this study, following the methods described in Tremblay et al.[13]
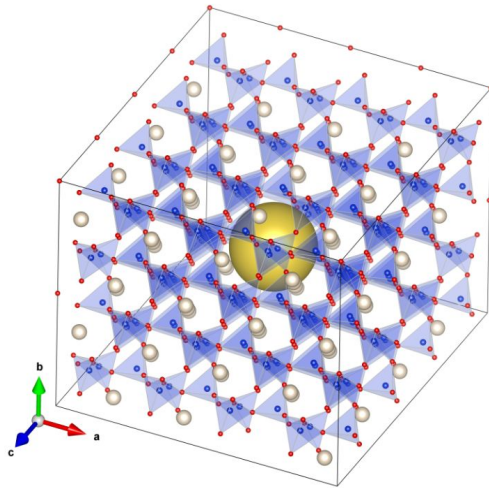
Figure 2. The quartz supercell showing the nanopore (yellow) and interstitial sites along the c-axis channels (white).
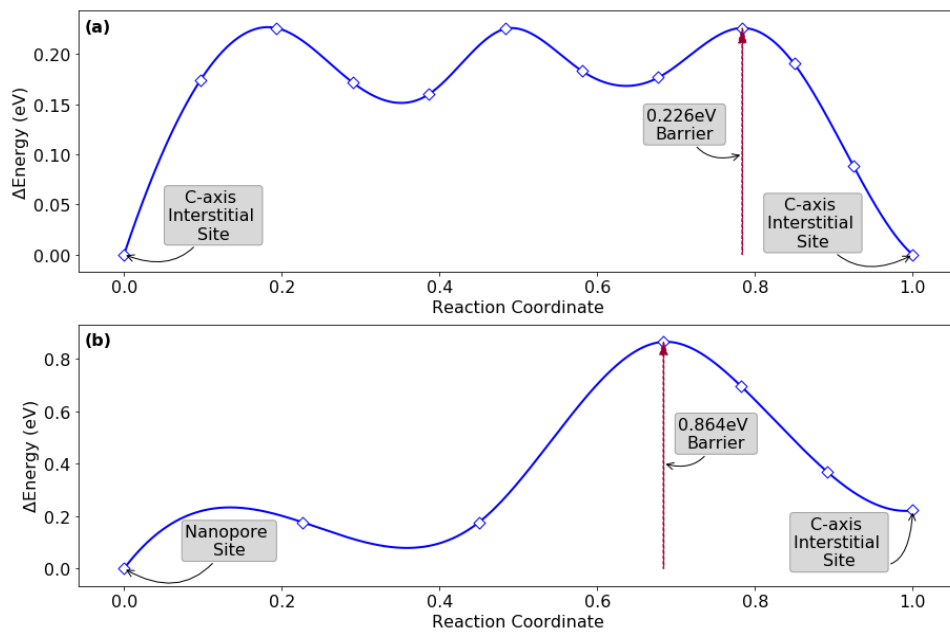
Figure 3. Helium atom energy as a function of reaction coordinate progress along the minimum energy diffusion path for perfect quartz (a), and quartz with a nanopore (b).
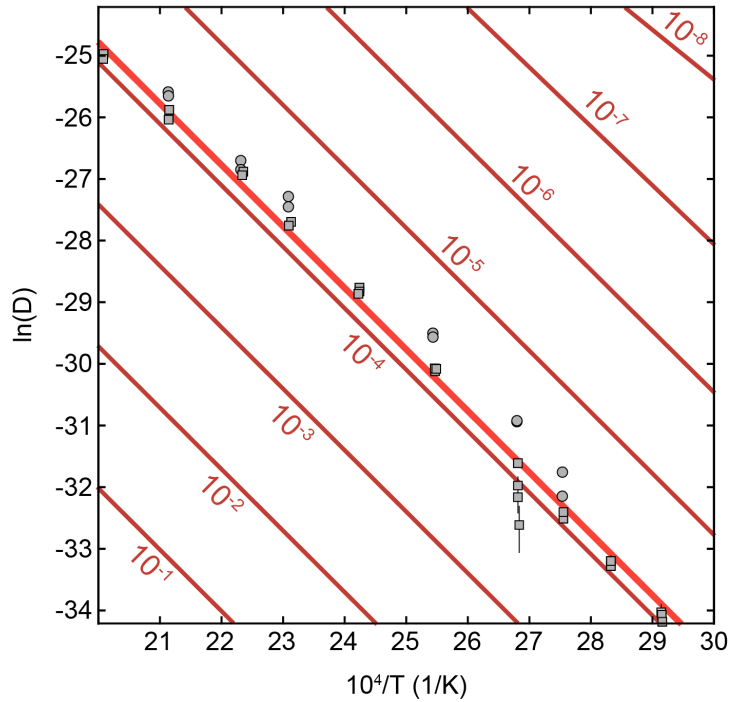
Figure 4. Data from the two laboratory experiments on gem-quality quartz sample GRR-1668 (gray symbols; this work and Shuster and Farley[3]), calculated assuming a spherical diffusion geometry. D values are normalized to m2s-1. Lines represent DFT-simulated diffusivities, calculated according to Eq. 2 for different fractions of diffusion steps out of nanopores and in the [001] direction. Each line is labeled with $f_{nanopore}$, except for the thick light red line which corresponds to $f_{nanopore} = 7.2 \times 10^{-5}$ and which minimizes the reduced χ^2 misfit with the experimental data.
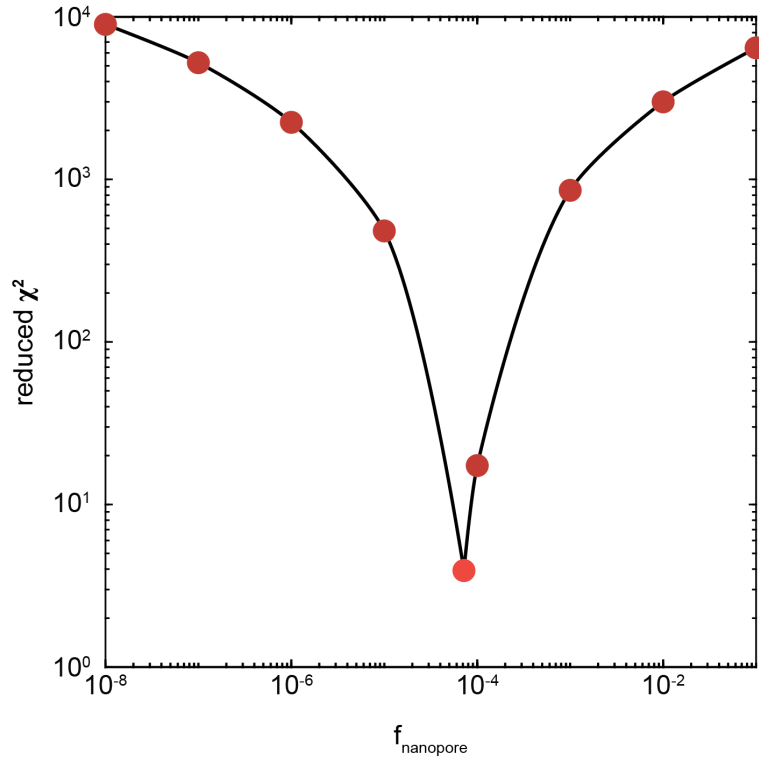
Figure 5. Reduced χ2 misfit for the $f_{nanopore}$ values in Figure 4 with respect to the experimental data.

Table 1. Step-degassing measurements for the replicate helium diffusion experiment on gem-quality quartz sample GRR-1668. 'bdl' stands for below detection limit.

Step	Temperature (º C)	± (º C)	Duration (hours)	^{3}He (× 10^6 atoms)	± (× 10^6 atoms)	Diffusivity (m²/s)
1	90.02	0.51	1.00	82.68	1.62	1.09×10^{-14}
2	90.00	1.35	2.00	75.59	1.35	1.62×10^{-14}
3	100.02	0.52	1.00	52.82	1.33	3.66×10^{-14}
4	100.01	0.47	1.75	66.92	1.35	3.72×10^{-14}
5	120.04	0.67	0.50	58.91	1.45	1.54×10^{-13}
6	120.02	0.53	1.00	82.67	1.46	1.45×10^{-13}
7	160.02	0.55	0.50	225.98	2.43	1.41×10^{-12}

8	160.01	0.42	1.00	178.47	2.12	1.20×10^{-12}
9	175.03	0.56	0.50	91.29	1.28	2.53×10^{-12}
10	175.02	0.50	0.75	55.78	1.37	2.19×10^{-12}
11	200.02	0.46	0.50	35.45	1.08	7.71×10^{-12}
12	199.94	3.87	0.75	5.08	0.39	4.92×10^{-12}
13	224.90	5.32	0.50	0.33	0.10	–
14	225.01	0.36	1.00	bdl	bdl	–
15	250.01	0.44	0.50	bdl	bdl	–
16	250.00	0.32	1.00	bdl	bdl	–
17	275.01	0.35	0.50	bdl	bdl	–
18	275.00	0.28	1.00	bdl	bdl	–
19	300.01	0.32	0.50	bdl	bdl	–
20	300.00	0.26	1.00	bdl	bdl	–
21	324.99	0.50	0.50	bdl	bdl	–
22	349.98	0.35	0.50	bdl	bdl	–
23	349.99	0.30	1.00	bdl	bdl	–

Table 2. Helium diffusion kinetic parameters in quartz determined with DFT calculations. Diffusion directions are listed for the perfect quartz crystal.

Direction	E_a (eV)	E_a (kJ/mol)	Transition Rate (THz)	D_0 (m²/s)
[100]	0.571	54.9	9.25	2.23×10^{-6}
[010]	0.574	55.1	9.06	2.19×10^{-6}
[001]	0.226	21.8	12.84	3.75×10^{-6}
Nanopore	0.864	82.9	2.17	5.69×10^{-7}

Table 3. Fraction of diffusion steps in different crystallographic directions and out of nanopores that minimize the reduced χ^2 misfit (χ^2 per degree of freedom) with experimentally-determined diffusivities per Eq. 2. We calculate experimental diffusivities assuming both a spherical and infinite sheet diffusion geometry. While a spherical geometry has typically been assumed for quartz in laboratory experiments (e.g., Shuster and Farley[3], Tremblay et al.[13]) the strong anisotropy in the [001] direction implied by the DFT results suggests that an infinite sheet geometry may be more appropriate. For consistency with Shuster and Farley[1], Figures 1 and 4 show the spherical geometry. For completeness, we report DFT results that minimize the reduced χ^2 misfit for the following conditions: (1) diffusion out of nanopores and [001] sites only, (2) diffusion out of nanopores and in all 3 crystallographic directions, and (3) diffusion in all 3 crystallographic directions with no nanopores, i.e. perfect quartz.

Geometry	$f_{[001]}$	$f_{[100]}$	$f_{[010]}$	$f_{nanopore}$	Reduced χ^2
(1) sphere	0.9999	–	–	7.2×10^{-5}	3.9×10^{0}
(2) sphere	0.9942	0.0020	0.0037	7.2×10^{-5}	5.2×10^{0}
(3) sphere	0.0082	0.0129	0.9789	–	1.8×10^{2}
(1) sheet	0.9999	–	–	9.9×10^{-6}	2.3×10^{1}
(2) sheet	0.9641	0.0251	0.0108	9.2×10^{-6}	2.1×10^{0}
(3) sheet	0.5129	0.0083	0.4863	–	2.6×10^{2}

SUPPORTING INFORMATION

Derivation of Eq. 2.

REFERENCES

(1)   Reiners, P. W.; Ehlers, T. A.; Zeitler, P. K. Past, Present, and Future of Thermochronology. *Reviews in Mineralogy and Geochemistry* **2005**, *58* (1), 1–18. https://doi.org/10.2138/rmg.2005.58.1.

(2)   Tremblay, M. M.; Shuster, D. L.; Balco, G. Cosmogenic Noble Gas Paleothermometry. *Earth and Planetary Science Letters* **2014**, *400*, 195–205. https://doi.org/10.1016/j.epsl.2014.05.040.

(3)   Shuster, D. L.; Farley, K. A. Diffusion Kinetics of Proton-Induced ^{21}Ne, ^{3}He, and ^{4}He in Quartz. *Geochimica et Cosmochimica Acta* **2005**, *69* (9), 2349–2359. https://doi.org/10.1016/j.gca.2004.11.002.

(4)   Cherniak, D. J.; Watson, E. B.; Thomas, J. B. Diffusion of Helium in Zircon and Apatite. *Chemical Geology* **2009**, *268* (1–2), 155–166. https://doi.org/10.1016/j.chemgeo.2009.08.011.

(5)   Guenthner, W. R.; Reiners, P. W.; Ketcham, R. A.; Nasdala, L.; Giester, G. Helium Diffusion in Natural Zircon: Radiation Damage, Anisotropy, and the Interpretation of Zircon (U-Th)/He Thermochronology. *American Journal of Science* **2013**, *313* (3), 145–198. https://doi.org/10.2475/03.2013.01.

(6)   Shuster, D. L.; Flowers, R. M.; Farley, K. A. The Influence of Natural Radiation Damage on Helium Diffusion Kinetics in Apatite. *Earth and Planetary Science Letters* **2006**, *249* (3–4), 148–161. https://doi.org/10.1016/j.epsl.2006.07.028.

(7)   Flowers, R. M.; Ketcham, R. A.; Shuster, D. L.; Farley, K. A. Apatite (U–Th)/He Thermochronometry Using a Radiation Damage Accumulation and Annealing Model. *Geochimica et Cosmochimica Acta* **2009**, *73* (8), 2347–2365. https://doi.org/10.1016/j.gca.2009.01.015.

(8)   Farley, K. A. Helium Diffusion from Apatite: General Behavior as Illustrated by Durango Fluorapatite. *Journal of Geophysical Research: Solid Earth* **2000**, *105* (B2), 2903–2914. https://doi.org/10.1029/1999JB900348.

(9)   Gautheron, C.; Tassan-Got, L.; Barbarand, J.; Pagel, M. Effect of Alpha-Damage Annealing on Apatite (U–Th)/He Thermochronology. *Chemical Geology* **2009**, *266* (3–4), 157–170. https://doi.org/10.1016/j.chemgeo.2009.06.001.

(10)   Gerin, C.; Gautheron, C.; Oliviero, E.; Bachelet, C.; Mbongo Djimbi, D.; Seydoux-Guillaume, A.-M.; Tassan-Got, L.; Sarda, P.; Roques, J.; Garrido, F. Influence of Vacancy Damage on He Diffusion in Apatite, Investigated at Atomic to Mineralogical Scales. *Geochimica et Cosmochimica Acta* **2017**, *197*, 87–103. https://doi.org/10.1016/j.gca.2016.10.018.

(11)   Saadoune, I.; Purton, J. A.; de Leeuw, N. H. He Incorporation and Diffusion Pathways in Pure and Defective Zircon ZrSiO4: A Density Functional Theory Study. *Chemical Geology* **2009**, *258* (3–4), 182–196. https://doi.org/10.1016/j.chemgeo.2008.10.015.

(12)   Gautheron, C.; Djimbi, D. M.; Roques, J.; Balout, H.; Ketcham, R. A.; Simoni, E.; Pik, R.; Seydoux-Guillaume, A.-M.; Tassan-Got, L. A Multi-Method, Multi-Scale Theoretical Study of He and Ne Diffusion in Zircon. *Geochimica et Cosmochimica Acta* **2020**, *268*, 348–367. https://doi.org/10.1016/j.gca.2019.10.007.

(13)   Tremblay, M. M.; Shuster, D. L.; Balco, G. Diffusion Kinetics of ^{3}He and ^{21}Ne in Quartz and Implications for Cosmogenic Noble Gas Paleothermometry. *Geochimica et Cosmochimica Acta* **2014**, *142*, 186–204. https://doi.org/10.1016/j.gca.2014.08.010.

(14)   Lin, K.-J.; Ding, H.; Demkowicz, M. J. Formation, Migration, and Clustering Energies of Interstitial He in α-Quartz and β-Cristobalite. *Journal of Nuclear Materials* **2016**, *479*, 224–231. https://doi.org/10.1016/j.jnucmat.2016.06.049.

(15)   Kresse, G.; Joubert, D. From Ultrasoft Pseudopotentials to the Projector Augmented-Wave Method. *Physical Review B* **1999**, *59* (3), 1758. https://doi.org/10.1103/PhysRevB.59.1758.

(16)   Henkelman, G.; Uberuaga, B. P.; Jónsson, H. A Climbing Image Nudged Elastic Band Method for Finding Saddle Points and Minimum Energy Paths. *The Journal of Chemical Physics* **2000**, *113* (22), 9901–9904. https://doi.org/10.1063/1.1329672.

(17)   Henkelman, G.; Jónsson, H. Improved Tangent Estimate in the Nudged Elastic Band Method for Finding Minimum Energy Paths and Saddle Points. *The Journal of Chemical Physics* **2000**, *113* (22), 9978–9985. https://doi.org/10.1063/1.1323224.

(18)   Jónsson, H.; Mills, G.; Jacobsen, K. W. Nudged Elastic Band Method for Finding Minimum Energy Paths of Transitions. In *Classical and quantum dynamics in condensed phase simulations*; World Scientific, 1998; pp 385–404.

(19)   Vineyard, G. H. Frequency Factors and Isotope Effects in Solid State Rate Processes. *Journal of Physics and Chemistry of Solids* **1957**, *3* (1–2), 121–127. https://doi.org/10.1016/0022-3697(57)90059-8.

(20)   Fechtig, H.; Kalbitzer, S. The Diffusion of Argon in Potassium-Bearing Solids. In *Potassium Argon Dating*; Springer Berlin Heidelberg: Berlin, Heidelberg, 1966; pp 68–107. https://doi.org/10.1007/978-3-642-87895-4_4.

(21)   Brook, E. J.; Kurz, M. D. Surface-Exposure Chronology Using in Situ Cosmogenic [3]He in Antarctic Quartz Sandstone Boulders. *Quaternary Research* **1993**, *39* (1), 1–10. https://doi.org/10.1006/qres.1993.1001.

(22)   Watson, E. B.; Cherniak, D. J. Lattice Diffusion of Ar in Quartz, with Constraints on Ar Solubility and Evidence of Nanopores. *Geochimica et Cosmochimica Acta* **2003**, *67* (11), 2043–2062. https://doi.org/10.1016/S0016-7037(02)01340-6.

(23)   Kovalenko, M. A.; Kupryazhkin, A. Y.; Gupta, S. K. Influence of Defects on the Diffusion of Helium in Uranium Dioxide: Molecular Dynamics Study. In *AIP Conference Proceedings*; AIP Publishing LLC, 2019; Vol. 2142, p 020002. https://doi.org/10.1063/1.5122325.

(24)   Bengtson, A.; Ewing, R. C.; Becker, U. He Diffusion and Closure Temperatures in Apatite and Zircon: A Density Functional Theory Investigation. *Geochimica et Cosmochimica Acta* **2012**, *86*, 228–238. https://doi.org/10.1016/j.gca.2012.03.004.

(25)   Djimbi, D. M.; Gautheron, C.; Roques, J.; Tassan-Got, L.; Gerin, C.; Simoni, E. Impact of Apatite Chemical Composition on (U-Th)/He Thermochronometry: An Atomistic Point of View. *Geochimica et Cosmochimica Acta* **2015**, *167*, 162–176. https://doi.org/10.1016/j.gca.2015.06.017.

(26)   Zeitler, P. K.; Enkelmann, E.; Thomas, J. B.; Watson, E. B.; Ancuta, L. D.; Idleman, B. D. Solubility and Trapping of Helium in Apatite. *Geochimica et Cosmochimica Acta* **2017**, *209*, 1–8. https://doi.org/10.1016/j.gca.2017.03.041.

(27)   McDannell, K. T.; Zeitler, P. K.; Janes, D. G.; Idleman, B. D.; Fayon, A. K. Screening Apatites for (U-Th)/He Thermochronometry via Continuous Ramped Heating: He Age Components and Implications for Age Dispersion. *Geochimica et Cosmochimica Acta* **2018**, *223*, 90–106. https://doi.org/10.1016/j.gca.2017.11.031.

For Table of Contents Only